THE SOLAR X-RAY LIMB

Marina Battaglia,[1] Hugh S. Hudson,[2,3] Gordon J. Hurford,[3] Säm Krucker,[1,3] and Richard A. Schwartz[4]

[1]*University of Applied Sciences and Arts Northwestern Switzerland, CH-5210 Windisch, Switzerland*
[2]*School of Physics and Astronomy, SUPA, University of Glasgow, Glasgow G12 8QQ, UK*
[3]*SSL, UC Berkeley, 7 Gauss Way, Berkeley, CA, USA*
[4]*Catholic University of America at NASA Goddard Space Flight Center, Greenbelt, MD 20771, USA*

ABSTRACT

We describe a new technique to measure the height of the X-ray limb with observations from occulted X-ray flare sources as observed by the RHESSI (the Reuven Ramaty High-Energy Spectroscopic Imager) satellite. This method has model dependencies different from those present in traditional observations at optical wavelengths, which depend upon detailed modeling involving radiative transfer in a medium with complicated geometry and flows. It thus provides an independent and more rigorous measurement of the "true" solar radius, meaning that of the mass distribution. RHESSI's measurement makes use of the flare X-ray source's spatial Fourier components (the visibilities), which are sensitive to the presence of the sharp edge at the lower boundary of the occulted source. We have found a suitable flare event for analysis, SOL2011-10-20T03:25 (M1.7), and report a first result from this novel technique here. Using a 4-minute integration over the 3-25 keV photon energy range, we find $R_{\mathrm{X-ray}} = 964.05 \pm 0.15 \pm 0.29$ arcsec, where the uncertainties include statistical uncertainties from the method and a systematic error. The standard VAL-C model predicts a value of 963.48 arcsec, about 2σ below our value.

Keywords: Sun, Sun:flares, Sun:X-rays

Corresponding author: Marina Battaglia
marina.battaglia@fhnw.ch

1. INTRODUCTION

We normally determine the outer boundary of the Sun by observations at optical wavelengths, essentially making use of the radial distance of the tangent ray for which the optical depth τ is unity at a standard wavelength, such as 5000 Å. Such a definition depends upon details of the atmospheric structure and of the physics of the radiative transfer (absorption and scattering) within that structure. The standard reference for the value, as cited by Allen (1973), appears to be the fundamental observational work of Auwers (1891), who made extensive visual observations with "heliometers." These were used to measure the angular separation between the two ends of a given solar diameter. The measurements gave the value 1919.26 ± 0.10 arcsec. A more recent standard was set by Brown & Christensen-Dalsgaard (1998), who used timing measurements of meridian transits in a special-purpose telescope operated between 1981 and 1987. This yielded a value of 1919.359 ± 0.018 arcsec for the observed near-equatorial diameter. These angular measures for the location of the solar limb need an adjustment to provide estimates of the solar radius itself, expressed in SI units, because the observed limb lies several scale heights above the physical radius. The current best value for the radius itself, incorporating many sources, gives $R_\odot = 695.658 \pm 140$ km (Haberreiter et al. 2008). This value has been rounded off and adopted within errors as the IAU nominal value $\mathcal{R}_\odot^{\mathrm{N}} = 695.7$ km (Prša et al. 2016) as one of a set of self-consistent values for solar and planetary properties.

What do such measurements mean physically? From the point of view of stellar structure, we may wish to use such a measurement to characterize the spatial distribution of the solar material, and so we would like to interpret the opacity measurement as a radial distance from Sun center, for example. For reference, the point in a semi-empirical atmospheric model such as VAL-C (Vernazza et al. 1981) corresponding to the nominal radial distance $R_\odot$ has optical depth $\tau_{5000\text{Å}} = 1$ as viewed radially from above. This optical depth conventionally defines the location of the photosphere, or the solar radius. According to the VAL-C model, the total mass of the atmosphere above that point is about 10^{-10} $M_\odot$, and so a sphere at this radial distance from Sun center (i.e., within $R_\odot$) contains most of the mass of the Sun. The increase of optical depth for oblique rays means that the observed limb always lies above the conventional photosphere. The difference amounts to several photospheric scale heights (about 350 km; see Brown & Christensen-Dalsgaard 1998; Haberreiter et al. 2008, for a discussion of this point). At longer and shorter wavelengths (relative to the "opacity minimum" at about 1.5 μm), the opacity generally increases, but its spectral behavior is greatly complicated by atomic and molecular transitions. The radial distance of the apparent limb thus generally increases as the opacity increases, slowly towards the infrared and more rapidly in the UV.

Because of the presence of flows and oscillations on small scales, the surface of the Sun is not smooth. The height of the limb thus depends on the dynamics of the upper solar atmosphere at a given wavelength, an interesting problem normally described by numerical models and relevant to such matters as the chemical composition (e.g., Asplund et al. 2009). Much literature (see, e.g., Rozelot et al. 2015) has been devoted to characterizing the limb and its dynamics at all wavelengths. In this paper we report a first attempt to make precise measurements of the X-ray limb, by a technique that is more directly related to the mass distribution, rather than to the opacity structure at longer wavelengths. The method is based on locating the sharp lower edge of partially-occulted flare sources as observed by

the Reuven Ramaty High-Energy Solar Spectroscopic Imager (RHESSI) spacecraft (Lin et al. 2002). The limb thus observed is in *absorption*, due to the photoeffect and Compton scattering. Photoelectric absorption, important below about 12 keV, depends upon the elemental abundances and the ionization state of the medium. At higher energies Compton scattering becomes dominant. In the scattering regime we have a particularly simple interpretation: the absorption ideally just depends upon the column density of electrons, free or bound, along the line of sight. RHESSI is well-suited to observing the sharp occulted edge of the source because of its natural interpretation in terms of discrete spatial Fourier components (Hurford et al. 2002), as discussed for this application in Section 2. Note that Wannier et al. (1983) used an analogous technique to study the limb at mm wavelengths. In Section 3 we describe observations of a single partially-occulted flare, chosen as the best case after extensive searches. The calculation of the limb height and comparison with predictions from models are given in Section 4.

2. VISIBILITY THEORY

RHESSI is a collimator-based Fourier imager. The incident photon flux from a solar flare is time-modulated by two grids as the spacecraft spins around its axis. RHESSI has nine detectors and, accordingly, nine pairs of grids (G1 through G9) with different pitch-widths corresponding to angular resolutions from as small as 2.26 arcsec in the case of G1 up to 183.2 for G9 (Lin et al. 2002; Hurford et al. 2002). Our technique converts the RHESSI time series of a given X-ray source into discrete two-dimensional Fourier components $V(u,v)$ that we call visibilities. The directness of the sensitivity of visibility-based techniques to an occulted source is suggested by the relation between visibilities and the spatial profile of a source. Let $I(x)$ be the intensity of a two-

dimensional source projected onto the x-axis. Then the relationship between the projected intensity and the set of visibilities $V(u)$, whose spatial frequencies u are in the x-direction, is given by:

$$V(u) = \int I(x) \exp(-2\pi iux)dx \qquad (1)$$

and therefore

$$I(x) = \int V(u) \exp(2\pi iux)du \ . \qquad (2)$$

This illustrates how the source profile can be reconstructed from a set of visibility measurements. Spatially differentiating Equation 2 yields

$$\frac{dI(x)}{dx} = 2\pi \int iuV(u) \exp(2\pi iux)du \qquad (3)$$

$$= 2\pi \int V_*(u) \exp(2\pi iux)du \ , \qquad (4)$$

which implies that the spatial derivative of the source profile, $I'(x) = dI(x)/dx$, can be reconstructed from a set of modified visibilities, $V_*(u) = iuV(u)$. The modified visibilities $V_*(u)$ are thus derived from the measured visibilities, $V(u)$, by applying a 90 degree phase shift (the factor i) and weighting by the spatial frequency u. $V_*(u)$ is given by

$$V_*(u) = \int I'(x) \exp(-2\pi iux)dx \ . \qquad (5)$$

Numerically evaluating Equation 1 for an unocculted Gaussian source profile results in the behavior shown by the black solid curve in Figure 1. As a smaller source becomes over-resolved at high spatial frequencies, the visibility amplitudes decrease rapidly. For a smooth source that is occulted abruptly at $x = x_0$, $I'(x)$ has a sharp peak – approaching a delta function for an arbitrarily sharp limb – and evaluating Equation 5 yields $V_*(u) = \exp(-2\pi iux_0)$, from which $V(u) = (1/iu) \times \exp(2\pi iux_0)$. In other words,
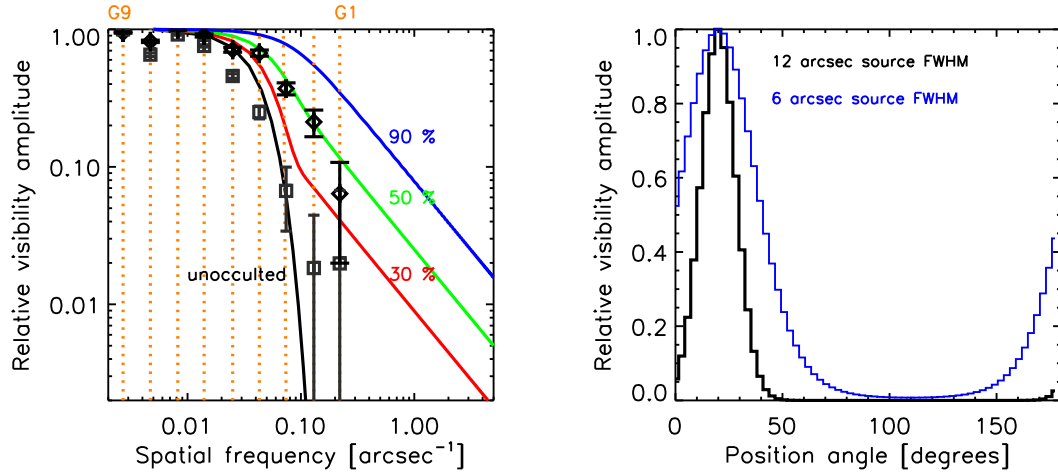
Figure 1. Left: relative amplitudes of visibilities corresponding to the sharp edge of a Gaussian source of FWHM = 12 arcsec which is occulted by different fractions (given as % in the Figure). The vertical dashed lines show the spatial frequencies of the RHESSI collimators. Diamonds are the relative visibility amplitudes associated with the limb signature in the event analyzed here. Rectangles give the relative amplitudes of the visibilities perpendicular to the limb. Right: the predicted visibility amplitude vs. rotational position angle for RHESSI collimator 1 (2.26″ FWHM), showing a prominent peak at the angle dictated by the limb orientation in the model, and with a Gaussian width determined by the collimator resolution and source size. Note that in reality the visibility amplitude at position angles perpendicular to the source will have a finite value, unlike the idealized case, due to statistical uncertainties and source sub-structure.

at high spatial frequencies we find a contribution to the visibility amplitude that decreases as 1/(spatial frequency). This is confirmed numerically in Figure 1 for various fractional occultations of a Gaussian source (colored solid lines). Note that the phase of this visibility depends on the location of the occulted edge of the source. As Figure 1 suggests, the presence of an occulted edge to an otherwise smooth source results in visibilities with significantly enhanced amplitudes at the higher spatial frequencies. However this enhancement applies only to visibilities whose spatial frequencies are orthogonal to the occulted edge. Thus the direct signature of occultation is a spike in the amplitudes of visibilities at high spatial frequencies, when the direction of these visibilities approaches orthogonality to the occulted edge of the source. This is illustrated in the right-hand part of Figure 1, where the visibility amplitudes as a function of position angle for two sources with 12 arcsec FWHM and 6 arcsec FWHM that are occulted

at an angle of 20 degrees are shown. Note how the width of the peak in amplitude depends on the source size. To summarize, visibility analysis allows us to distinguish the sharp, precisely oriented image edge expected from limb occultation, from other spatial structures intrinsic to the source. For this we have several tests:

1. There must be a peak in the high spatial frequency visibility amplitude as a function of position angle

2. The peak must occur at the position angle corresponding to the limb orientation

3. The peak should have an amplitude consistent with the expectation from the total visible source flux and the occultation fraction, while the amplitude of visibilities at other angles must show no such behaviour (compare Figure 1).
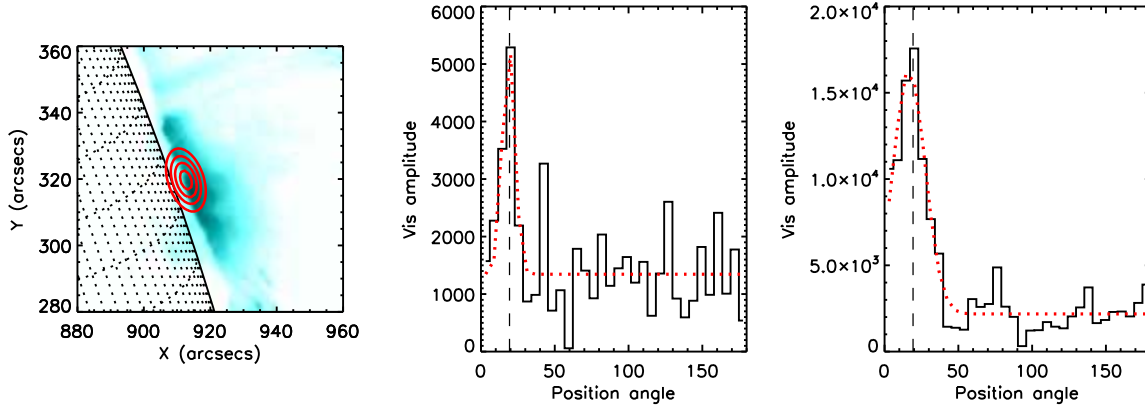
Figure 2. Left: AIA 131Å image of SOL2011-10-20T03:25, obtained in the middle of the RHESSI integration. The red contours give the 30%, 50%, 70%, and 90% contours of the RHESSI visibility forward fit at 3-25 keV over a four-minute time interval. Middle: Visibility amplitude versus position angle for collimator 1; note that we measure position angles CCW from the W limb in this case. The dashed line indicates the position angle of the limb at the flare location. Right: same as middle, but for collimator 2. The red dotted line gives a Gaussian fit to the data.

4. The peak should have width consistent with the source size and collimator pitch (see Figure 1)

5. The ratios of the peaks in different sub-collimators should be consistent with their relative spatial frequencies

These tests embody model-dependence and are not conclusive; for example if the actual solar limb had a tilt just on the size scale of the source, this would confuse Test 2.

3. OBSERVATIONS

Candidate flares for this application must not only be appropriately located and occulted, but their unocculted emission must be large enough to provide sufficient counting statistics for RHESSI. Note the trade-off with the depth of occultation, which results in a larger visibility enhancement (see Figure 1) but also lower observable emission. We have found an ideal candidate, SOL2011-10-20T03:25 (M1.7). Images from SDO/AIA at 131 Å suggest that the flare source was indeed occulted. In addition, RHESSI's detector 2 was performing well enough for its data to be used for this kind of

analysis, hence we can use the modulation of G2 as an independent measure. As a feasibility demonstration we have analyzed the visibilities over an energy band of 3-25 keV, and over the four-minute time interval from 03:15:00 – 03:19:00 UT, chosen to maximize the signal-to-noise ratio. RHESSI's G1, with a spatial resolution of 2.26″ (FWHM), and G2, with a resolution of 3.92″, have the highest spatial frequencies and so are best suited to observe the spike in visibility amplitude described in Section 2. Figure 2 shows a AIA 131 Å image overlaid with the RHESSI source. Because the signature of the occulted edge of the source is limited to a small azimuthal range for the highest resolution subcollimators, images made with "traditional" imaging algorithms cannot be readily interpreted in terms of the edge location and properties. In particular, none of the traditional imaging algorithms use an image basis appropriately optimized for an occulted source, but use some form of circular or Gaussian symmetry for the reconstruction. This is why we must use visibilities directly. The visibility amplitudes as a function of position angle

Table 1. Comparison of observed visibility amplitude properties of collimators 1 and 2 with expectation for a 12 arcsec FWHM source at 50% occultation.

Item	Test	Expectation	Observed	Pass/fail
1	Existence of peaks	Both G1 and G2	Yes	pass
2	Limb angle vs position of peak	identical	$19.3°$ vs $20°$	pass
3	Vis amplitude in G1	~ 8800 ph cm^{-2}s^{-1}	5377 ± 887 ph cm^{-2}s^{-1}	possible
3	Vis amplitude in G2	$\sim 1.7 \times 10^4$ ph cm^{-2}s^{-1}	$(1.6 \pm 0.1) \times 10^4$ ph cm^{-2}s^{-1}	pass
4	Width of peak in G1	20 deg	9.78 ± 2.20 deg	possible
4	Width of peak in G2	34 deg	25.5 ± 2.02 deg	possible
5	Ratio of max amplitude G1/G2	0.58	0.33 ± 0.25	pass

for collimators 1 and 2 (G1 and G2) are also shown in Figure 2.

We have applied the tests described in Section 2 to these observations. The first and most important test is that there be distinct peaks in both G1 and G2, at the correct location and well in excess of the uncertainty estimates derived from the point-by-point measurements of the complex amplitudes. The data clearly pass this test. Unfortunately the other tests have some ambiguities and uncertainties. Note that the expectations for these tests must refer to a model that may be inappropriate in some details. In particular, we do not know the actual width of the source nor the fraction by which it is occulted. A full image made via the visibility forward-fitting technique gives a FWHM of $11''$. Hence, for comparison, an occultation of 50% and a circular Gaussian source of FWHM 12 arcsec (giving a lower limit of the amplitude peak width) was used. Compared with this model, the observed peak is narrower (found by fitting a Gaussian to the observed amplitudes, red line in Figure 2) than expected. The ratio of the amplitudes is also lower than it should be, though has quite large uncertainties within which it agrees with the expectation. Note that the latter only depends on the relative spatial

frequencies of the grids used and not on the source properties. The results of the tests are summarized in Table 1. In addition to these tests we used the RHESSI simulation software (part of the Solar Software) to calculate the expected visibility amplitudes and phases in a more realistic way. The map center for the reconstructed visiblities was set to [908.8, 318.6] arcsec, the estimated location of the limb, the same as was used for the actual analysis. The resulting visibility amplitudes and phases for G1 and G2 are compared with the observed data in Figure 3. The simulations show a peak at the same location and with similar width as the observed data and also the phases agree well. In addition, the visibility amplitudes at position angles not associated with the limb display fluctuations of the same order as the observed visibility amplitudes, suggesting that these are predominantly due to statistical uncertainties, rather than source substructure. Finally, we have to exclude the possibility that the source is not occulted but thin and elongated along the limb, which would result in a similar visibility amplitude behaviour. As can be see in Figure 2, the visibility forward fit suggests an elongated source in the direction of the limb that would be consistent with a non-occulted elliptical source
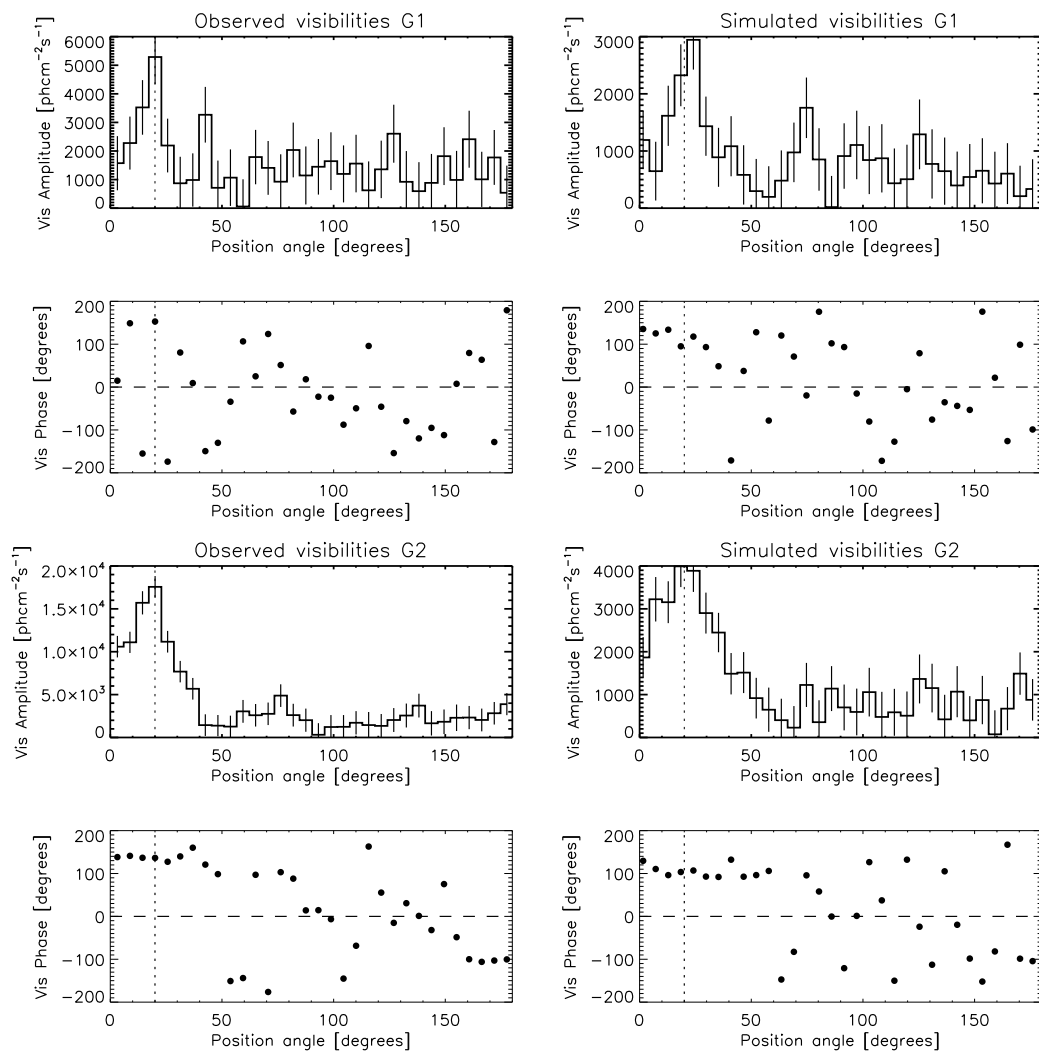
Figure 3. Comparison of observed visibility amplitudes and phases from grids 1 and 2 with simulations of a source with 12 arcsec FWHM that is 50% occulted. Left: observed data. Right: simulations. Top to bottom: Amplitudes and phases of collimator 1 (G1), amplitudes and phases of collimator 2 (G2).

with 15 arcsec FWHM large axis and a 8 arcsec FWHM short axis. In Figure 1 the observed relative amplitudes from the visibilities along the direction of the limb and perpendicular to the limb are shown. The data are clearly inconsistent with a non-occulted source, as the amplitudes in G1 and G2 are several orders of magnitude above the expectation for a non-occulted source and for an 8 arcsec source extent perpendicular to the limb, the difference would be even more pronounced.

In summary the observations clearly pass tests number 1, 2, and 5, which are independent of the source morphology and occultation fraction. The results of tests 3 and 4 are a bit ambiguous, as these depend on a model of the true source whose morphology is not known. In addition, simulations show a similar behaviour as the observations, and we can exclude a thin, non-occulted source parallel to the limb. Thus we interpret the observed spike in amplitude as reflecting the limb edge and analyze its complex amplitudes to derive the limb height in the following.

4. OBSERVED AND PREDICTED LIMB HEIGHT

4.1. *Limb height from visibility analysis*

For a given subcollimator, the information on the radial position R_L of the limb is contained in the phase ϕ of the complex visibility, where

$$R_L = C_M + \frac{(\phi_L - \pi/2)}{2\pi} \times p, \qquad (6)$$

where $C_M = \sqrt{x_c^2 + y_c^2}$ is the position of the map-center used for the visibility calculation, and p is the pitch of the collimator that is used for the analysis (4.52 arcsec for G1 and 7.84 arcsec for G2 which are used here). The location of the map center is determined by the metrology of the RHESSI grid optics (essentially, the RHESSI plate scale). Figure 4 shows the visbilities of G1 and G2 in the complex plane, the

basis of the analysis. The visibility phase is the angle measured counter-clockwise from the positive x-axis, the amplitude is the radial distance from the origin of the coordinate system. The visibilities that are dominated by the limb signal were identified as the points around the peak with an amplitude larger than its 3σ uncertainty. They are summed up vectorially to give the phase that represents the limb signal. From this, the vectorial sum of all other visibilities ("background") was subtracted. The resulting phase was then used in Equation 6 to calculate the radial limb position. The mean limb location, derived in this way from the observed phase information, is given in Table 2. We show two sets of errors: the formal errors of the visibility fit, based explicitly upon the counting statistics, and a second set estimating the systematic error. The former is derived from the uncertainty of the phase measurement. Note that, even though the resolution of the grids is limited to a few arcseconds, the visibility phases can be measured with much higher accuracy (compare Figure 4). The systematic uncertainty consists of three components. The first one uses the empirical scatter of the significant phase measurements at our binning, i.e. the standard deviation of the visibility phases associated with the limb (red points in Figure 4). For the weighted mean we also incorporate two possible instrumental uncertainties: the length of the metering tube that holds the grids, and the accuracy of the Sun-center determination from the solar aspect system. For the former we adopt a 3σ error of $0.026''$ (Zehnder et al. 2003), and for the latter, as an upper limit, $0.15''$ (Fivian et al. 2002).

4.2. *Predictions*

Figure 5 displays our result in terms of height of the observed limb above the photosphere in comparison with the height of the visible limb. Given the fundamental difference between an X-ray absorption signature of the limb
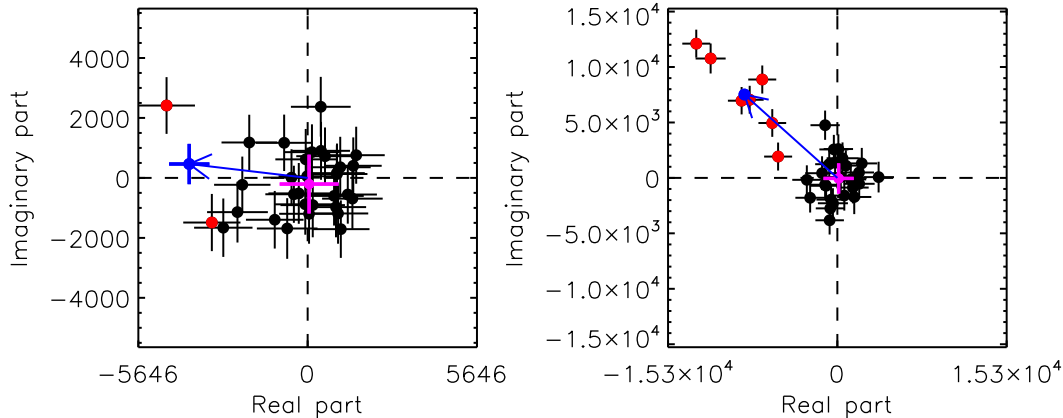
Figure 4. Observed visibilities in G1 (left) and G2 (right) in the complex plane. The red dots give the presumed limb signal with an amplitude larger than 3σ of its uncertainty. The purple point gives the vectorially added background visibilities. The blue point and arrow give the phase of the limb.

Table 2. Mean limb location for SOL2011-10-20T:03:25, integrated over photon energy range of 3-25 keV. The uncertainties of the measurement are given as statistical uncertainties from the visibility fit plus systematic uncertainties.

Collimator	FWHM ($''$)	Result ($''$)
G1	2.26	$964.04 \pm 0.41 \pm 0.46$
G2	3.92	$964.05 \pm 0.16 \pm 0.21$
Weighted mean (G1+G2)		$964.05 \pm 0.15 \pm 0.29$
Prediction		963.55 (10 keV)

location, its visible location, and the known wavelength-dependence of the solar radius (e.g. Rozelot et al. 2015), our results are within expectation regarding the difference between X-ray limb height and optical limb. We also compare the observed limb height with the predicted X-ray limb height from a model atmosphere. For this first result we compare with the standard VAL-C semi-empirical model atmosphere (Vernazza et al. 1981). We have calculated the X-ray opacity of the photospheric plasma from weighted means of the mass attenuation coeffi-

cients of the contributing elements (H, He, C, N, O, and Fe), incorporating both the photoelectric effect and electron (Compton) scattering. Note that this approach omits any fine structure associated with flows (leading to corrugations), and sphericity. The predicted limb height varies with photon energy, as shown in Figure 5 for the photospheric solar elemental abundances of Caffau et al. (2011) and lies below the observed height with a 2σ significance (see Section 5). The electron scattering just depends upon the total line-of-sight electron den-

sity, including atomic electrons, at X-ray photon
energies. The photoeffect, on the other hand,
depends upon the bound-state populations of
different ionic states, and requires a detailed
model. We have assumed negligible ionization
in the photosphere, and spherical symmetry, to
determine the impact factor for 1/e attenuation
of the occulted source. Note that the predicted
height only varies slowly with photon energy
above the Fe K-edge (visible as discontinuity at
7 keV in Figure 5), because of the dominance
of electron scattering for X-ray opacity in the
photosphere. Nevertheless the Fe feature does
reveal itself significantly, so that with better ob-
servations one could obtain a clean determina-
tion of a mean Fe abundance in this way.

5. DISCUSSION

The technique we have explored in analyz-
ing the RHESSI observations of SOL2011-10-
20T03:25 (M1.7) has a particularly simple phys-
ical interpretation in terms of the actual mass
distribution with height in the atmosphere. De-
spite this, and despite the excellent opportunity
that the RHESSI rotating modulation collima-
tors afford, we regard this first result as a tenta-
tive one. Partly this is because of the difficulty
of finding suitable occulted flares bright enough
for this analysis, but mainly it is for systematic
reasons that we discuss here.

Several factors contribute, the most impor-
tant in this case being the relative locations
of the pointing axis (a few arcminutes west of
Sun center), Sun center, and the flare location.
The measurement of visibilities whose orienta-
tion matches the direction of a line from the
pointing axis to the limb source can be compro-
mised by incomplete phase sampling (Figure 4
of Hurford et al. 2002). This factor could be al-
leviated by non-uniform pointing variations (at
the relevant roll angle) on a scale of a few arc-
seconds. Unfortunately in this case, RHESSI's
pointing was too stable. For visibilities tan-
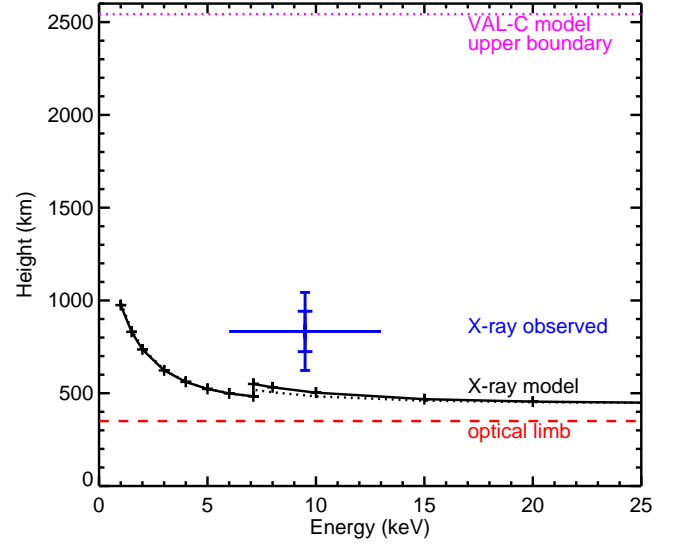gent to the limb, there is no problem because

Figure 5. Prediction of the occultation height
in the VAL-C model atmosphere (Vernazza et al.
1981) as a function of X-ray energy, making use of
abundances from Caffau et al. (2011). The dotted
line shows the same calculation for coronal abun-
dances (Schmelz et al. 2012). The dashed line gives
a standard estimate for the height of the optical
limb. Our measurement and its uncertainties (sta-
tistical and systematic) are given as the blue cross,
which is centered at the peak of the RHESSI count
spectrum. The horizontal bar indicates the FWHM
of the count spectrum peak, which is significantly
narrower than the energy range used to make visi-
bilites (3-25 keV). These estimates assume neutral
plasma and spherical symmetry.

of the rapid variation of the modulation. Other
lesser problems with the data include the sim-
ple problem of counting statistics: only a small
fraction of the data apply to just the visibil-
ity components needed. Finally, the theoretical
visibility pattern depends to a certain extent
on unknown fine-scale image structure that may
compete with the sharp edge expected for the
occultation.

Why is the measured X-ray limb location
above its predicted height? Of course, the pre-
diction requires model assumptions. In particu-
lar our prediction ignores the presence of phys-
ical corrugations of the limb (Simon & Zirin

1969; Gu et al. 1997). The structures would need to be in excess of the hydrostatic scale height of about 100 km in the photosphere, and on small angular scales. The likeliest sources for such corrugations would be p-mode or convective flows in the photosphere (Kuhn et al. 2000) or some lower-atmosphere counterpart of the spicule structure seen in the chromosphere (e.g. Ewell et al. 1993; Ayres 2002). We think it unlikely that they have an influence on the model or observations, based on present knowledge, but look forward to higher-resolution optical observations and to more definitive modeling.

Other issues have to do with possible time variability of the limb location, as well as the physical nature of the particular patch of the Sun involved in our single determination; a quiet-Sun model such as VAL-C may simply be inappropriate. Such a local interpretation might also help to resolve the unexpectedly low altitude found for the hard X-ray sources in a single well-observed flare on the visible hemisphere (Martínez Oliveros et al. 2012). The Sun itself may be aspherical, but we note that the observed oblateness term is not large enough to be relevant here (Fivian et al. 2008).

6. CONCLUSION

The results presented here, to our knowledge the first X-ray measurements of the solar radius, offer great promise. In spite of the caveats discussed above, we are optimistic that this technique can generate a rigorous and independent measurement of the true solar radius: the X-ray measurements provide a means to determine the actual mass distribution rather than the more model-dependent distribution of opacity that underlies classical optical techniques. The result (Table 2) does not quite match expectations from the standard VAL-C model, even within errors. The discrepancy between observation and prediction, at about 2σ significance, could imply errors in our use of the VAL-C model, for example by application to an area of the Sun near a major active region. Corrugations of the atmosphere at these temperature-minimum heights could also play a role. The technique is sound enough for us to encourage further exploration of the RHESSI database for this purpose, with the ultimate goal of establishing better solar radius determinations this way. If this becomes possible, improved observations using the X-ray technique could in principle help determine solar iron abundance, taking advantage of the effect of the K-edge visible in Figure 5.

REFERENCES

Allen, C. W. 1973, Astrophysical quantities, ed. Allen, C. W.

Asplund, M., Grevesse, N., Sauval, A. J., & Scott, P. 2009, ARA&A, 47, 481

Auwers, A. 1891, Astronomische Nachrichten, 128, 361

Ayres, T. R. 2002, ApJ, 575, 1104

Brown, T. M., & Christensen-Dalsgaard, J. 1998, ApJL, 500, L195+

Caffau, E., Ludwig, H.-G., Steffen, M., Freytag, B., & Bonifacio, P. 2011, SoPh, 268, 255

Ewell, Jr., M. W., Zirin, H., Jensen, J. B., & Bastian, T. S. 1993, ApJ, 403, 426

Fivian, M., Hemmeck, R., McHedlishvili, A., & Zehnder, A. 2002, SoPh, 210, 87

Fivian, M. D., Hudson, H. S., Lin, R. P., & Zahid, H. J. 2008, Science, 322, 560

Gu, Y., Jefferies, J. T., Lindsey, C., & Avrett, E. H. 1997, ApJ, 484, 960

Haberreiter, M., Schmutz, W., & Kosovichev, A. G. 2008, ApJL, 675, L53

Hurford, G. J., Schmahl, E. J., Schwartz, R. A., et al. 2002, SoPh, 210, 61

Kuhn, J. R., Armstrong, J. D., Bush, R. I., & Scherrer, P. 2000, Nature, 405, 544

Lin, R. P., Dennis, B. R., Hurford, G. J., et al. 2002, SoPh, 210, 3

Martínez Oliveros, J.-C., Hudson, H. S., Hurford, G. J., et al. 2012, ApJL, 753, L26

Prša, A., Harmanec, P., Torres, G., et al. 2016, AJ, 152, 41

Rozelot, J. P., Kosovichev, A., & Kilcik, A. 2015, ApJ, 812, 91

Schmelz, J. T., Reames, D. V., von Steiger, R., & Basu, S. 2012, ApJ, 755, 33

Simon, M., & Zirin, H. 1969, SoPh, 9, 317

Vernazza, J. E., Avrett, E. H., & Loeser, R. 1981, ApJS, 45, 635

Wannier, P. G., Hurford, G. J., & Seielstad, G. A. 1983, ApJ, 264, 660

Zehnder, A., Bialkowski, J., Burri, F., et al. 2003, in Proc. SPIE, Vol. 4853, Innovative Telescopes and Instrumentation for Solar Astrophysics, ed. S. L. Keil & S. V. Avakyan, 41–59